

Bis[1]benzothieno[1,4]thiazine-S-oxides—Luminescence of the Anti-Anti-Regioisomer

Simone T. Hauer, J. Maurice Pütz, Christian Ganter, Thomas J. J. Müller

Article - Version of Record



Suggested Citation:

Hauer, S., Pütz, J. M., Ganter, C., & Müller, T. J. J. (2025). Bis[1]benzothieno[1,4]thiazine-S-oxides—Luminescence of the Anti-Anti-Regioisomer. *Asian Journal of Organic Chemistry*, 14(8), Article e00490. <https://doi.org/10.1002/ajoc.202500490>

Wissen, wo das Wissen ist.



UNIVERSITÄTS- UND
LANDESBIBLIOTHEK
DÜSSELDORF

This version is available at:

URN: <https://nbn-resolving.org/urn:nbn:de:hbz:061-20250911-115318-2>

Terms of Use:

This work is licensed under the Creative Commons Attribution 4.0 International License.

For more information see: <https://creativecommons.org/licenses/by/4.0>

Bis[1]benzothieno[1,4]thiazine-S-oxides–Luminescence of the *Anti-Anti*-Regioisomer

Simone T. Hauer,^[a] J. Maurice Pütz,^[b] Christian Ganter,^[b] and Thomas J. J. Müller*^[a]

Three regioisomeric *N*-para-fluorophenyl bis[1]benzothieno[1,4]-thiazines (BBTT) are selectively oxidized under mild conditions to give the corresponding BBTT-S-oxides, which were fully characterized by single crystal structural analysis. The newly formed S-oxide is uniformly oriented in a pseudo-axial *S-extra* position, whilst the *N*-aryl substituent adopts an *N-intra* conformation. In comparison to the diminished planarization of the BBTT scaffold

according to DFT calculations, the structures are considerably planarized in the crystal. Only the *anti-anti*-BBTT-S-oxide emits intensively and the electronic structure of the absorption and emission spectra can be elucidated by TDDFT calculations. This blue emission, both in solution ($\Phi_f = 17\%$) and in the solid state ($\Phi_f = 66\%$), is significant and qualifies this isomer as an attractive emitter.

1. Introduction

Carbo- and heterocyclic donor π -systems are important constituents in organic electronics, photonics, and photovoltaics.^[1–12] Particularly favorable are reversible low oxidation potentials, which render tri(hetero)arylamines and their derivatives to be promising hole conducting molecules.^[13–19] While low oxidation potentials of donor molecules promise facile oxidation to radical cations, the high lying HOMOs indicate a strong donor capacity for functional chromophores, especially luminescent systems. Dithieno[1,4]thiazines can be considered as electron-density-enriched, tunable congeners of phenothiazines.^[20,21] Due to their lower oxidation potentials and higher radical cation stability, they outperform phenothiazine as novel types of donors for organic chromophores and electrophores.^[22]

This benzo-versus-thieno exchange can be even conceptualized further by inserting the thieno anellation between the benzo rings and the central 1,4-thiazine core, leading to pentacyclic bis[1]benzothieno[1,4]thiazines (BBTT) (Figure 1).^[23]

BBTTs have become highly interesting functional π -systems due to their considerably lower oxidation potentials than phenothiazines, their increased stability of the radical cations, and the significant red-shifted emission, as well as their increased planarized electronic structure for *anti-anti*-isomers, which can be attributed to an increased antiaromatic character.^[24,25] Even expanded systems with remarkably enhanced luminescence characteristics can be obtained by organometallic cross-coupling methodology.^[26]

For transmitting the enhanced planarization of *anti-anti*-BBTTs, and thereby the antiaromatic character, from the crystalline solid state into solution phase behavior, we recently introduced the conformationally enforced planarization of the central 1,4-thiazine by *ortho,ortho'*-disubstitution of the *N*-aryl substituent that already adopts an *N-intra* (pseudo-equatorial) conformation.^[27] This rational design of conformational planarization, initiated by systematic DFT and TDDFT calculation, also causes the predicted change of the electronic structure of the ground and excited states in solution.

In a previous work, we chose the regioisomeric *N*-para-fluorophenyl-BBTTs *syn-syn*-BBTT 1, *syn-anti*-BBTT 2, and *anti-anti*-BBTT 3 for studying their stepwise one-electron oxidation to radical cations $1^{\cdot+}$, $2^{\cdot+}$, and $3^{\cdot+}$, and even dications 1^{2+} , 2^{2+} , and 3^{2+} (Scheme 1), preparatively as their hexachloroantimonates and by spectroelectrochemistry (UV–vis) characterizing the antimonates by EPR for the paramagnetic radical cations and by NMR spectroscopy for the diamagnetic dications.^[28] Their electronic structures were unambiguously assigned by restricted and unrestricted DFT and TDDFT calculations. This prompted us to explore another mode of oxidation of these anellated 1,4-thiazines, leading to diamagnetic oxidation products, namely to the corresponding sulfoxides (S-oxides). Given the dominance of the electron density in the central 1,4-thiazine core, this encouraged us to probe the chemoselective oxidation of all three isomers to the corresponding BBTT-S-oxides, and to study the structural, electronic (absorption and emission) characteristics in comparison to their native BBTT precursors.

[a] Dr. S. T. Hauer, Prof. Dr. T. J. J. Müller
Institut für Organische Chemie und Makromolekulare Chemie,
Heinrich-Heine-Universität Düsseldorf, Universitätsstraße 1, Düsseldorf
D-40225, Germany
E-mail: ThomasJJ.Mueller@hhu.de

[b] Dr. J. M. Pütz, Prof. Dr. C. Ganter
Institut für Anorganische Chemie und Strukturchemie,
Heinrich-Heine-Universität Düsseldorf, Universitätsstraße 1, Düsseldorf
D-40225, Germany

Dedication in Memory of Professor Masahiko Iyoda

Supporting information for this article is available on the WWW under
<https://doi.org/10.1002/ajoc.202500490>

© 2025 The Author(s). Asian Journal of Organic Chemistry published by Wiley-VCH GmbH. This is an open access article under the terms of the Creative Commons Attribution License, which permits use, distribution and reproduction in any medium, provided the original work is properly cited.

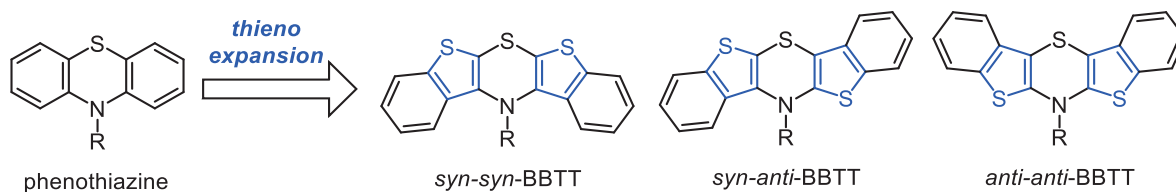
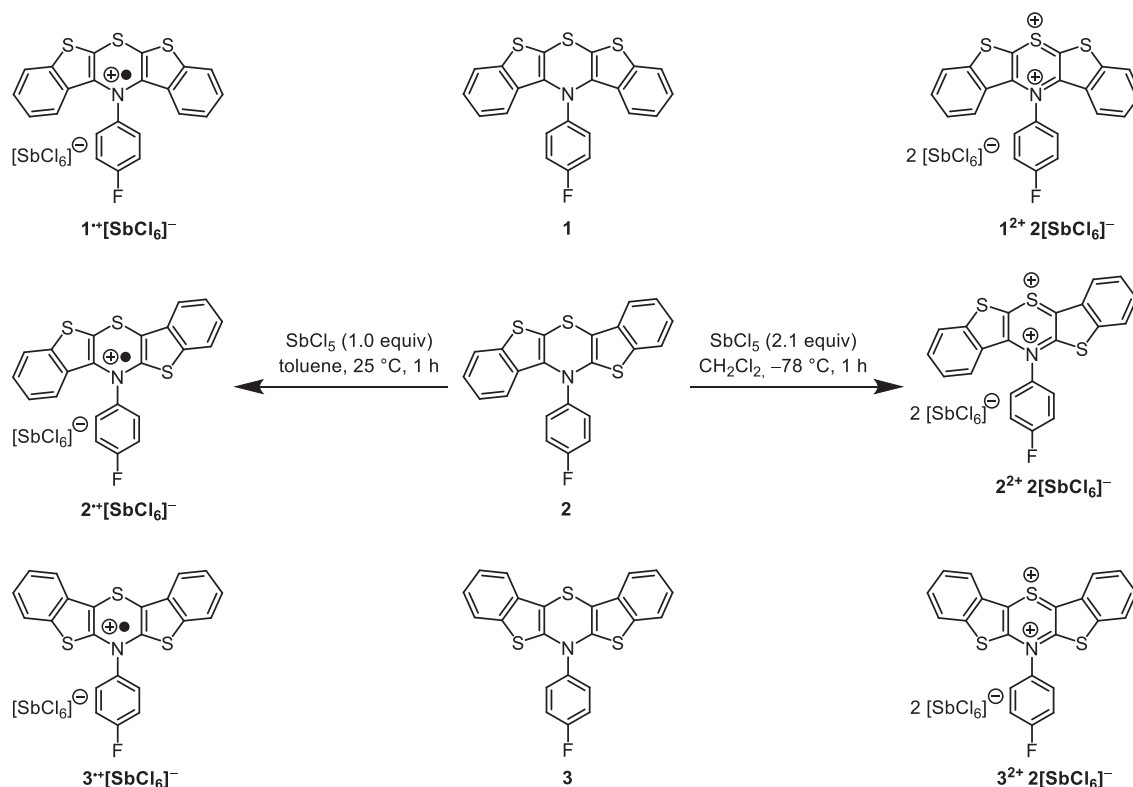


Figure 1. Formal twofold thieno expansion of phenothiazine to regioisomeric bis[1]benzothieno[1,4]thiazines (BBTTs).



Scheme 1. Selective synthesis of oxidized BBTT-compounds 1^+ , 2^+ , 3^+ , and 1^{2+} , 2^{2+} , 3^{2+} as their hexachloroantimonates.

2. Results and Discussion

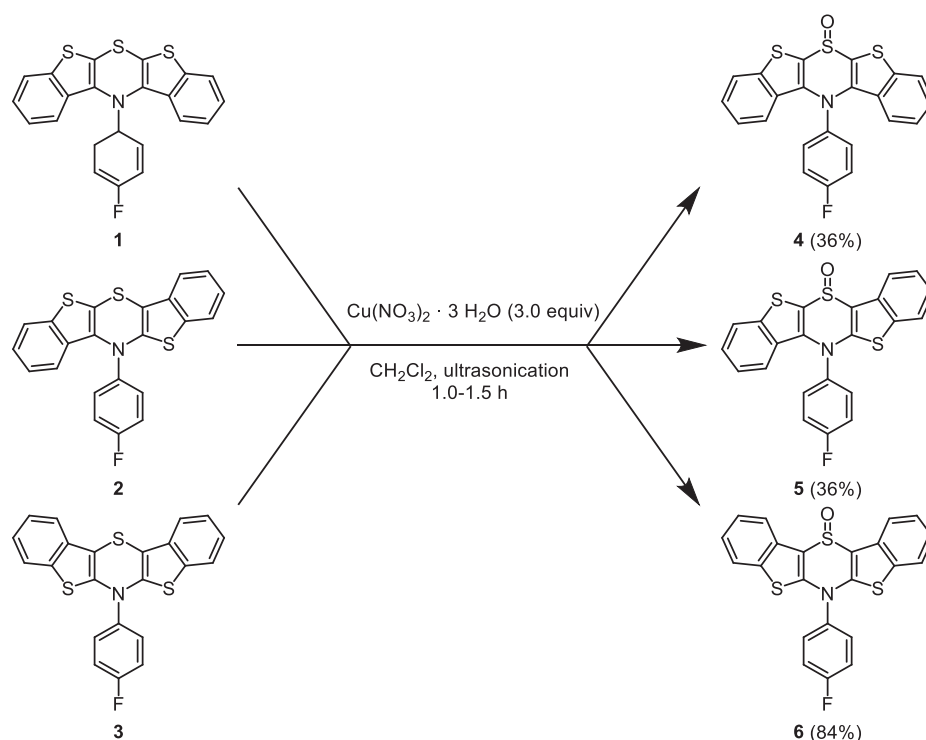
2.1. Synthesis of BBTT-S-oxides

The chemoselective oxidation of *N*-para-fluorophenyl-BBTT regioisomers *syn-syn*-BBTT **1**, *syn-anti*-BBTT **2**, and *anti-anti*-BBTT **3** can be achieved under mild conditions with copper(II) nitrate trihydrate in an ultrasound bath in analogy the synthesis of phenothiazine-*S*-oxides^[29] to give, after filtration and recrystallization from ethanol, the corresponding *syn-syn*-BBTT-*S*-oxide (**4**), *syn-anti*-BBTT-*S*-oxide (**5**), and *anti-anti*-BBTT-*S*-oxide (**6**) in 36–84% yield (Scheme 2). The structures of the target compounds were assigned by comprehensive NMR spectroscopy and mass spectrometry, and the molecular composition was determined by combustion analysis. The NMR spectra show the expected single set of signals, indicating the C_s symmetry of compounds **4** and **6**, as well as that only a single diastereomer was selectively formed upon oxidation in each case.

2.2. Structural Elucidation of the BBTT-S-oxides and Comparison to Calculated Structures

In addition, the structures of compounds **4**, **5**, and **6** were unambiguously corroborated by X-ray structure analyses (Figure 2).^[30,31] The asymmetric unit contains one molecule in each case. As already derived from NMR-spectroscopy, the sulfoxide is localized on the central 1,4-thiazine ring for all derivatives **4–6**, that is, the thieno-sulfur atoms of the annellated thiophenes do not undergo oxidation under the employed reaction conditions.

For all three BBTT-*S*-oxides **4–6**, the molecular structures reveal that the introduced oxygen atoms on the thiazine sulfur center adopt an *S-extra* (pseudo-axial) conformation, whereas the *N*-para-fluorophenyl substituents on the nitrogen atoms are placed in the *N-intra* (pseudo-equatorial) conformation. The lone pairs on the 1,4-thiazine sulfur atoms in native compounds **1**, **2**, and **3** are expectedly electronically nonequivalent,



Scheme 2. The sulfoxides of *syn-syn*-, *syn-anti*-, and *anti-anti*-*N*-*para*-fluorophenyl-BBTT 4, 5, and 6 by oxidation with copper(II) nitrate.

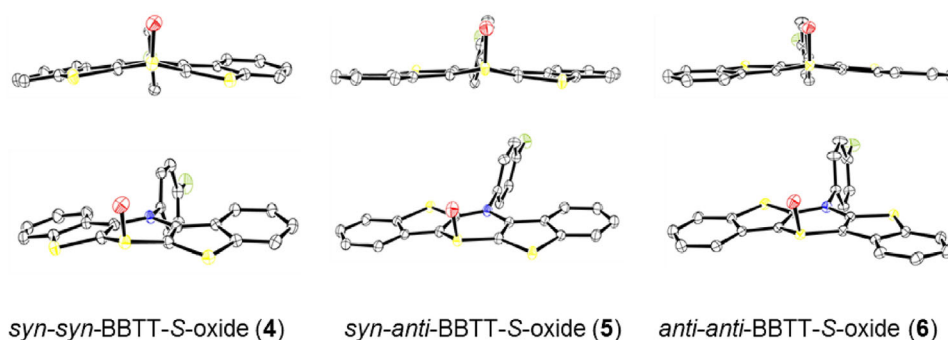


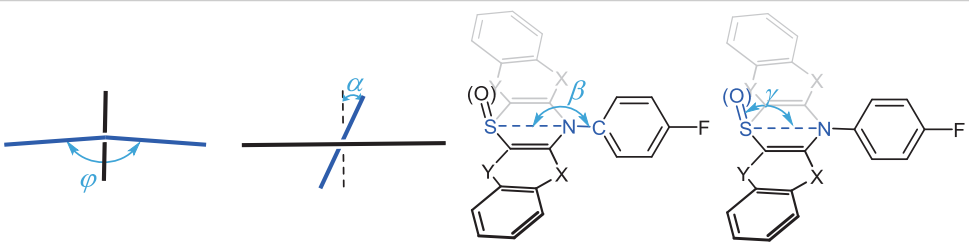
Figure 2. Molecular structures of BBTT-S-oxides 4, 5, and 6 in the frontal (top) and lateral view (bottom) in their respective asymmetric units (thermal ellipsoids are shown with 50% probability, whereby all hydrogen atoms are omitted for clarity).^[31]

and the lone pair in conjugation with the π -systems of the adjacent benzothiophenes is higher in energy and, therefore, the oxidation occurs even stereoselectively giving rise to the axially oriented *S-extra* oxide in all three cases. This agrees with the oxidation of phenothiazines, for example, sulfoxides of levomepromazine and chlorpromazine, where also the *S-extra* oxides were observed by single crystal structure analysis.^[32] In addition, the lack of π -overlap upon oxidation causes two electronic effects: (a) the antiaromatic character vanishes as the cyclic conjugation of $4n$ π -electrons is suspended with concomitant increase in planarization of the pentacyclic scaffold with extended π -conjugation, and (b) the sulfoxide can exert an electron-withdrawing effect as a part of an 1,4-thiazine-S-oxide. This overall planarization of the BBTT scaffold on the sulfoxides causes an almost orthogonal twist of the *N-para*-

fluorophenyl substituents. The orthogonal conformation is a consequence of the diminished steric repulsion and is clearly favored with the increased planarization in BBTT-S-oxides. This also becomes apparent by comparing *syn-syn*- (1) and *syn-anti*-BBTT (2), where the *N*-aryl substituents preferably adopt *N-extra* conformations as seen in the X-ray structures caused by a high steric repulsion,^[25] with the corresponding BBTT-S-oxides 4 and 5, where, by increased folding angles (Table 1) and therefore reduced steric repulsion, now *N-intra* conformations are clearly favored. A similar conformational change upon oxidation to the sulfoxides has been reported in the case of *N*-monodesmethyl chlorpromazine and chlorpromazine.^[32]

In addition, optimization of the geometry of sulfoxides 4, 5, and 6 in the gas phase^[33–38] with Gaussian 09^[39] (B3LYP functional^[40,41] and 6–311++G** basis set^[42–46]) support the

Table 1. Folding angles φ , torsional angles α , S—N—C_{aryl} alignment angles β and N—S—O bending angles γ of precursor BBTTs 1, 2, 3, and sulfoxides of BBTTs 4, 5, and 6 as extracted from crystal structure analysis and DFT calculations (B3LYP/6-311++G**).



Compound	Folding Angle φ		Torsion Angle α		S—N—C _{aryl} Angle β		N—S—O Angle γ	
	exp.	calcd.	exp.	calcd.	exp.	calcd.	exp.	calcd.
<i>syn-syn</i> -BBTT (1) ^{a)}	125.8°	130.0°	88.9°	26.7°	120.6°	114.9°	—	—
<i>syn-anti</i> -BBTT (2) ^{a)}	166.0°	144.8°	34.3°	20.8°	136.5°	127.6°	—	—
<i>anti-anti</i> -BBTT (3) ^{a)}	159.2° ^{b)}	148.0°	3.3° ^{b)}	0.0°	168.5° ^{b)}	160.2°	—	—
	155.6° ^{c)}		20.0° ^{c)}		167.1° ^{c)}			
<i>syn-syn</i> -BBTT-S-oxide (4)	168.2°	168.1°	5.7°	0.0°	179.7°	165.6°	90.8°	99.7°
<i>syn-anti</i> -BBTT-S-oxide (5)	175.5°	159.5°	12.3°	11.8°	164.8°	154.2°	108.1°	120.8°
<i>anti-anti</i> -BBTT-S-oxide (6)	171.3°	159.5°	3.9°	0.0°	170.2°	167.9°	112.0°	102.7°

^{a)} As reported in ref. 25. ^{b)} Molecule I in the elementary cell. ^{c)} Molecule II in the elementary cell.

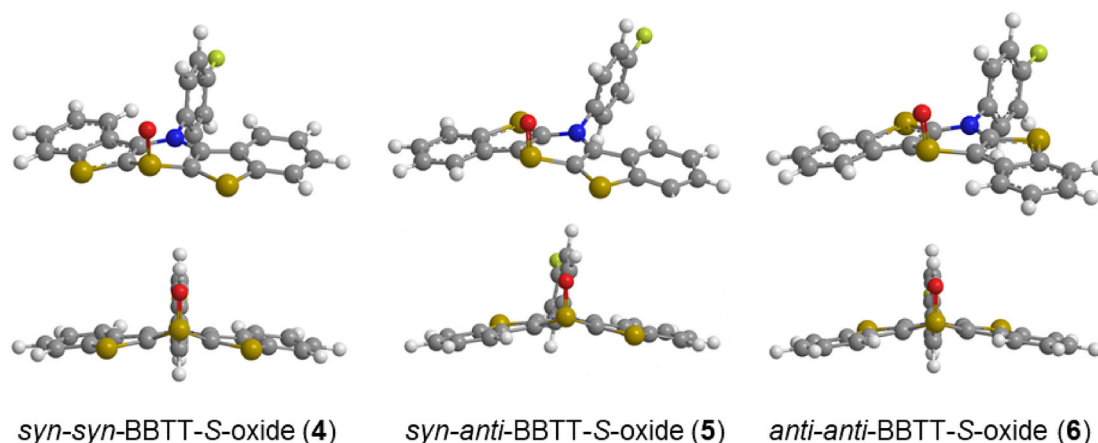


Figure 3. DFT-calculated (B3LYP/6-311++G**, gas phase) minimum structures of BBTT-S-oxides 4, 5, and 6 in the frontal (top) and lateral views (bottom).

N-intra-S-(oxide)-extra conformers as the preferred minimum structures (Figure 3, Table 1). The computational assessment of other minimum conformers remained unsuccessful, as no corresponding minima were found on the potential hypersurface. A potential scan with variation of the N—S—O angle γ , that is, the sulfoxide angle, also failed.

The calculated and experimentally assessed conformations of the isomers can be described by discussing interplanar dihedral angles φ and α as well as angles S—N—C_{aryl} (β) and N—S—O (γ).^[24,25] While the experimentally found folding angle φ of *syn-syn*-BBTT-S-oxide (4) is in good agreement (168.2°) with the calculated value (168.1°), the calculated minimum structures of the *syn-anti* (5) and *anti-anti* (6) isomers predict a stronger folding (159.5° and 159.5°) than experimentally found values

(175.5° and 171.3°). The calculated S—N—C_{aryl} angle β deviates more strongly from the values extracted from the X-ray structure analyses in the sense of a more tilted orientation of the *N*-aryl moiety for *syn-syn* (4) and *syn-anti* (5), whereas the calculated and experimental angle β of *anti-anti* (5) are quite similar. Therefore, increased planarization in the crystal lattice in comparison to the calculated structures can be attributed to packing effects.^[25] In contrast to the precursor molecules 1, 2, and 3, the calculated and experimentally assessed torsion angles α are found in a narrow range between 0.0° and 12.3°, caused by adaptation of the *N*-intra conformation of the *para*-fluorophenyl substituent. Similarly, the experimentally determined N—S—O angles γ in a range between 90.8 and 112.0° cum grano salis match with the calculated values.

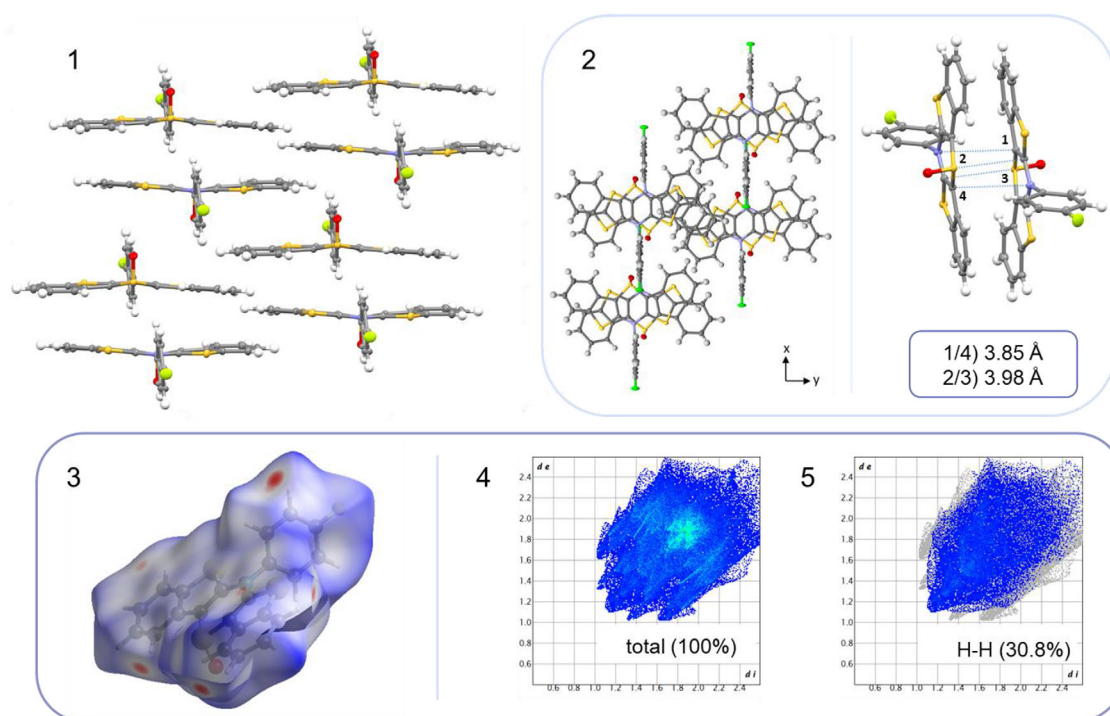


Figure 4. (1) Side view of the crystal packing of BBTT-S-oxide **6**. (2) Top view of the crystal packing of BBTT-S-oxide **6** (left) and distances between two molecules **6** (right).^[47] (3) Hirshfeld surface of sulfoxide **6** with the corresponding 2D fingerprint diagrams (4) of all total contacts and of (5) the relative H–H contacts.^[48]

To gain a better understanding of the induced planarization in the crystal, the crystal packings of the sulfoxides **4**, **5**, and **6** were examined with respect to possible intermolecular interactions, in particular strong π – π -interactions or hydrogen bond contacts. A comparable picture for all three regioisomers, exemplified for compound **6** (the discussion of the crystal packings of BBTT-S-oxides **4** and **5** is summarized in the [Supporting Information](#)), indicates pairwise or paired packing patterns of the BBTTs' scaffolds of two molecules in the lattice (Figure 4, inset 1).^[47] The pairwise packed molecules are mutually aligned with the *N*-aryl units oriented in opposite directions. In addition, the BBTTs' scaffolds are mutually arranged with their concave faces (Figure 4, inset 2). For the sulfoxide **6**, the view from the top shows that both molecules are in complete superposition, yet with a slight shift in direction of the self-selected *y*-axis. The largest intermolecular distances occur between the central 1,4-thiazines of those two paired molecules, with values of ≤ 3.98 Å. In contrast, the smallest distance of 3.30 Å is found between carbon atoms of the *b*-fusion side of one benzo[*b*]thiophene and the other. These fairly close contacts of π -systems give a first rationalization of the induced BBTT planarization in the crystal lattice.

The intermolecular interactions of the supramolecular packing were analyzed using the CrystalExplorer program by extracting the Hirshfeld surfaces and associated fingerprint diagrams.^[48] These encode the spatial interactions between the individual molecules in the crystal packing via the normalized contact distance d_{norm} of the atoms using a color code (Figure 4, insets 3). Intermolecular proximity between atoms that is smaller

than the sum of their van der Waals radii is highlighted in red on the surface, that is, short contacts. Intermolecular proximities of the sum of the van der Waals radii of the atoms involved are colored white. A progressive blue shift in coloring, turning light blue to dark blue, on the other hand, represents growing intermolecular proximities larger than the sum of the van der Waals radii of the atoms involved.

The fingerprint diagrams extract these intermolecular interactions as a plot of the distance of the Hirshfeld surface to the nearest nucleus outside the surface (d_e) against the distance of the Hirshfeld surface to the nearest nucleus inside the surface (d_i) in a simple 2D plot (Figure 4, insets 4 and 5). In addition to the total proportion of all contacts, the selected interactions between individual core identities can also be extracted.^[48–50] For BBTT-S-oxide **6**, some notable contacts between two cores below the sum of their van der Waals radii can be revealed (Figure 5). These results primarily from the spatial proximity between the aryl hydrogen atoms of different pairs, as can be seen by the red areas in the Hirshfeld surface and by the large proportion of H–H contacts in the total contacts of the corresponding fingerprint diagram. Short contacts also occur in the area of the oxygen atom of the sulfoxide, originating from a pair of neighboring hydrogen atoms. On the one hand, a short contact stems from a hydrogen atom of the *N*-aryl substituent of the equilaterally aligned molecule. On the other hand, there is also a short contact to a hydrogen atom of the benzo moiety of the BBTT's scaffold with the mutually oriented molecule of the pair. Even if the intermolecular distances of 2.344 Å (O–H) and 3.125 Å (O–C), as well as 2.413 Å (O–H) and 3.447 Å

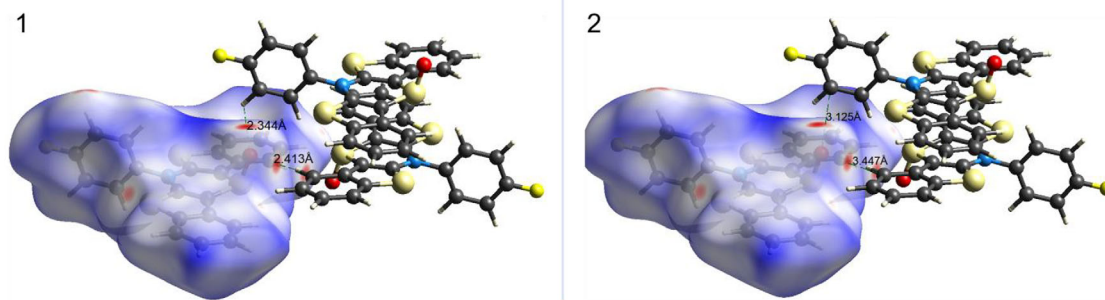


Figure 5. Graphical representation of selected short contacts (1) O—H and (2) C—O between two different pairs in the crystal of BBTT-S-oxide **6**.^[48]

(O—C) are in the acceptable range of weaker non-conventional hydrogen bonds with an aryl C—H group as a donor, the occurrence of hydrogen bonds cannot be assumed on the basis of the mutual arrangement of the individual molecules. The lone pair of the oxygen atom is not approximately linearly aligned with the corresponding C—H bond of the potential donor fragment.^[51]

For the rest of the Hirshfeld surface, in particular above and below the BBTT's scaffold, the atoms predominantly converge close to the sum of their van der Waals radii. The distances of carbon atoms with van der Waals radii of 1.70 Å should be in the range of 3.40 Å.^[52] This is in line with the previously discussed intermolecular distances between the BBTTs' scaffolds with values of 3.30–3.98 Å. This is also reflected in the fingerprint diagram of the total contacts by the light blue areas in the region at 1.8–2.0 d_i to 1.8–2.0 d_e . Consequently, according to a crystallographic definition, π – π interactions are plausible in the region of the fused benzo rings. However, these π – π interactions do not extend over the entire BBTT's scaffold as a consequence to the inherent folding along the S–N axis. All this supports the substantial influence of π – π interactions in inducing planarization.

For all BBTT-S-oxides **4**, **5**, and **6**, a pairwise arrangement with distances in the region of the van der Waals radii of two carbon nuclei of 3.40 Å is found, accompanied by a significantly diminished butterfly structure in the crystal structure. This diminishing is least pronounced for the sulfoxide **4** due to the smallest superposition of the BBTTs' scaffolds between the pairs of molecules in the crystalline solid state. In this light, the induced planarization of the precursor molecules **2** and **3** can also be discussed.^[25] The comparison of two polymorphs of *syn-anti-N-para*-fluorophenyl-BBTT (**2**) reveals that a significant increase in their folding angle φ from 136.5° to 166.0° might originate from a change in their packing pattern. While a more planarized conformation coincides with a pairwise arrangement in the crystal, the more folded conformers in the other polymorph are accompanied by a packing pattern with a non-paired arrangement of the molecules. Similarly, for the *anti-anti*-regioisomers, comparison of differently substituted *N-para*-phenyl-substituted BBTTs (R = F, CN, ^tBu or H) reveals that a more folded conformation in the crystal solid state is accompanied by a packing pattern of a non-paired arrangement, as for structure **3** (φ = 155.5 and 159.2°). In contrast, the crystal packing patterns of structure **6** with a paired-like alignment

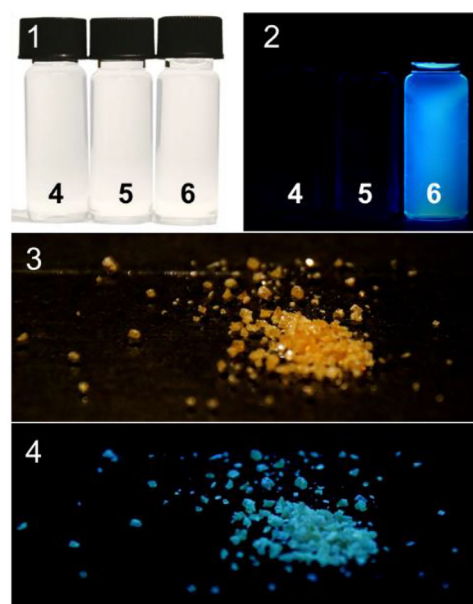


Figure 6. Solutions of BBTT-S-oxides **4**, **5**, and **6** (1) in daylight and (2) under irradiation with UV light (in CH₂Cl₂, $T = 298$ K, $c = 10^{-4}$ M, $\lambda_{exc} = 366$ nm). Crystals of BBTT-S-oxide **6** (3) in daylight and (4) under irradiation with UV light ($T = 298$ K, $\lambda_{exc} = 366$ nm).

show a stronger planarization with folding angles between 175.0° to 179.6°.

2.3. Optoelectronic Properties of BBTT-S-oxides and Calculated Electronic Structure

Under daylight the BBTT-S-oxides **4**, **5**, and **6** are colorless in solution (Figure 6, inset 1) and colorless, light yellow, or light orange in the crystalline solid state (Figure 6, inset 3), and compound **6** fluoresces strongly blue upon excitation with the handheld UV lamp ($\lambda_{exc} = 366$ nm), both in solution (Figure 6, inset 3) and in the solid state (Figure 6, inset 4). Therefore, the photophysical properties of BBTT-S-oxides **4**, **5**, and **6** were studied by UV–vis absorption and emission spectroscopy (Figure 7, Table 2).

The absorption spectra in dichloromethane show a pronounced longest wavelength absorption band around 340 nm in the UV region of the spectrum for all three dyes with extinction coefficients $\epsilon(\lambda)$ between 11 000 and 59 500 L·mol^{−1}·cm^{−1}, very

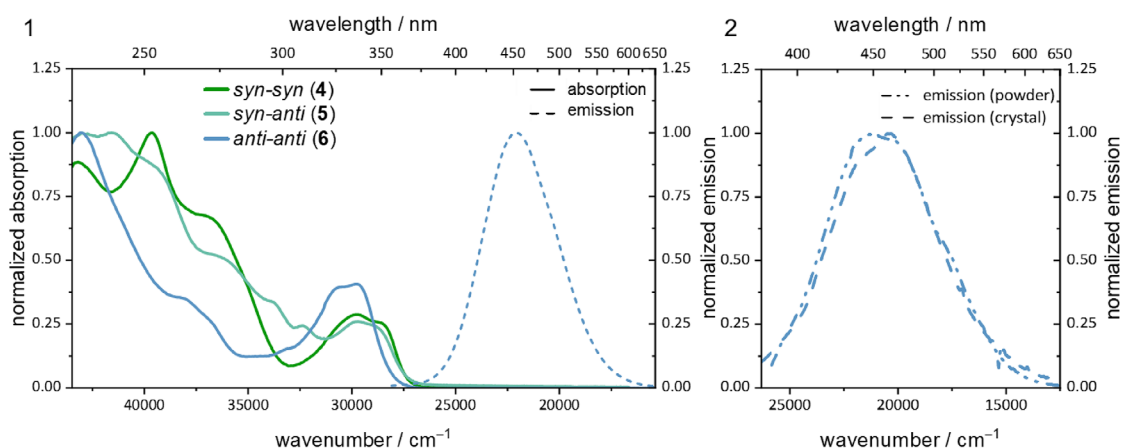


Figure 7. (1) UV-vis absorption (solid lines) and emission spectra (dashed line) of BBTT-S-oxides **4**, **5**, and **6** (recorded in CH₂Cl₂, $T = 298\text{ K}$, $c = 10^{-6}$ – 10^{-5} M for absorption; $c = 10^{-7}$ – 10^{-6} M for emission). (2) Emission spectra of powder (dashed-dotted line) and crystal (dashed line) of BBTT-S-oxide **6** ($T = 298\text{ K}$).

Table 2. Spectroscopic data of BBTT-S-oxides 4 , 5 , and 6 (recorded in CH ₂ Cl ₂ , $T = 298\text{ K}$, $c = 10^{-7}$ – 10^{-5} M).		
compound	$\lambda_{\text{max,abs}}$ [nm] (ϵ [L·mol ⁻¹ ·cm ⁻¹])	$\lambda_{\text{max,em}}$ [nm] ($\Delta\nu$ [cm ⁻¹], Φ_f)
4 (<i>syn-syn</i>)	232 (36 000), 252 (41 000), 271 (27500sh), 336 (12 000), 351 (10000sh)	—
5 (<i>syn-anti</i>)	232 (41 500), 240 (42 000), 255 (35500sh), 276 (21500sh), 297 (13500sh), 309 (10 000), 336 (11 000)	—
6 (<i>anti-anti</i>)	232 (149 000), 262 (51500sh), 325 (57000sh), 336 (59 500)	453 (7700, 0.17)

similar to the UV-vis spectra of BBTTs **1**, **2**, and **3**.^[24,25] Similarly as BBTT **1**, also BBTT-S-oxide **4** displays no measurable emission. While BBTT **2** only weakly emits, for BBTT-S-oxide **5**, no emission can be detected. Similarly, as for BBTT **3**, an intense emission at 453 nm with a Stokes shift of 7700 cm⁻¹ is found for BBTT-S-oxide **6**.^[24,25]

For compound **6**, the luminescence quantum yield Φ_f amounts to 0.17 in solution and to 0.66 in the crystalline powder. In comparison to precursor **3**, the emission band of BBTT-S-oxide **6** appears at 492 nm and is hypsochromically shifted in dichloromethane by 3700 cm⁻¹ and in the crystal by 3300 cm⁻¹. The emission band of the single crystalline material is even more blue-shifted and appears at 471 nm.

For assigning the experimentally observed longest wavelength absorption bands and the emission maximum in solution, the electronic structure was calculated for the *N*-intra, *S*-extra minimum conformers of BBTT-S-oxides **4**, **5**, and **6** obtained by geometry optimization (vide supra) on the (TD)DFT level of theory with B3LYP as the functional and 6-311++G** as the basis set,^[39] employing explicit simulation of the solvation shell using PCM (Polarizable Continuum Model) with the variation IEFPCM for dichloromethane as a dielectric (Table 3).^[53–56] The calculated transitions for the absorption are in very good agreement with the experimentally determined maxima for all

three regioisomers. The decreasing extinction coefficients $\epsilon(\lambda)$ with increasing bathochromic shift of the absorption bands are well reproduced by the relative magnitudes of the calculated oscillator strengths. The comparison also consistently reflects the experimentally significantly larger extinction coefficients $\epsilon(\lambda)$ of dye **6** compared to those of dyes **4** and **5** in theory through significantly increased oscillator strengths. The computations also reveal that the longest wavelength absorption bands of BBTT-S-oxides **4**, **5**, and **6** can be accounted to vertical S_1 states caused by HOMO→LUMO transitions with a quota of 96–98%.

The electronic structure of the longest wavelength transitions can be illustrated by Kohn-Sham frontier molecular orbitals (FMOs), that is, HOMO–LUMO (Figure 8). The distribution of the coefficient density reveals distinct differences for the three regioisomers **4**, **5**, and **6**. While BBTT-S-oxide **4** primarily shows localization of the coefficient density in the HOMO on the central 1,4-thiazine and the sulfur atoms of the thiophenes, the coefficient density of the HOMOs of BBTT-S-oxides **5** and **6** is completely distributed over the whole BBTTs' scaffold. In none of the three regioisomers coefficient density in the HOMO is found on the *N*-aryl moiety. The coefficient density distribution of the LUMOs of regioisomers **4** and **5** reveals a minor charge-transfer character of the HOMO→LUMO transitions. While for isomer **4** the coefficient density of the LUMO extends over the entire BBTT's scaffold, for isomer **5**, predominantly the *syn*-annellated wing is populated. Regioisomer **6** displays no charge-transfer character of the HOMO→LUMO transition, since the coefficient density of the LUMO is also distributed over the entire BBTT's scaffold. Again, for all BBTT-S-oxides **4**, **5**, and **6**, the LUMOs bear no coefficient density on the *N*-aryl moieties. The comparative analysis of the Kohn-Sham FMOs furthermore reveals a significantly larger HOMO–LUMO overlap integral for dye **6** than for dyes **4** and **5**. This is additionally reflected in the magnitude of the oscillatory strength of this transition of dye **6** (vide supra) in agreement with Fermi's Golden Rule.^[57]

Finally, for intensively luminescent BBTT-S-oxide **6**, the emission band was calculated on the TDDFT level of theory

Table 3. Experimental absorption maxima and selection of their underlying TDDFT-calculated transitions (B3LYP/6-311++G**, IEFCPCM CH₂Cl₂) of the BBTT-S-oxides **4**, **5**, and **6**.

	$\lambda_{\text{abs,exp}} [\text{nm}]$	$\lambda_{\text{abs,calcd}} [\text{nm}]$	Oscillator Strength	Most Dominant Contributions
<i>syn-syn</i> (4)	351	340	0.106	HOMO→LUMO (96%)
	336	330	0.111	HOMO→LUMO + 1 (97%)
	271	288	0.212	HOMO-1→LUMO (96%)
		270	0.090	HOMO→LUMO+ 7 (58%)
	252	263	0.230	HOMO→LUMO+ 5 (53%)
		250	0.153	HOMO-4→LUMO (6%)
		238	0.262	HOMO-4 →LUMO+ 2 (32%)
	232	233	0.169	HOMO-4 →LUMO+ 2 (36%)
		231	0.159	HOMO→LUMO + 11 (48%)
<i>syn-anti</i> (5)	336	337	0.217	HOMO→LUMO (97%)
	309	312	0.015	HOMO→LUMO+ 1 (97%)
		288	0.381	HOMO→LUMO + 3 (57%)
	276	278	0.056	HOMO→LUMO+ 4 (35%)
		256	0.237	HOMO-4→LUMO (29%)
		255	0.076	HOMO→LUMO+ 7 (39%)
		255	0.109	HOMO-1→LUMO+ 3 (49%)
	255	251	0.098	HOMO-2→LUMO+ 1 (64%)
		244	0.107	HOMO-2→LUMO+ 2 (49%)
	240	240	0.094	HOMO-1→LUMO + 6 (40%)
<i>anti-anti</i> (6)	232	235	0.135	HOMO-1→LUMO+ 4 (28%)
	336			
	325	325	0.573	HOMO→LUMO (98%)
	262	286	0.052	HOMO-1→LUMO (79%)
		260	0.056	HOMO→LUMO+ 4 (41%)
		258	0.050	HOMO-2→LUMO (36%)
		251	0.132	HOMO-4→LUMO (37%)
	232	234	0.176	HOMO-4→LUMO+ 1 (65%)
		233	0.426	HOMO-1→LUMO+ 7 (78%)

employing the minimum structure of the vibrationally relaxed excited S_1 state. The experimental value of 453 nm is reproduced to a good approximation with a calculated value of 478 nm. On the basis of the TDDFT calculation, a Jablonski diagram can be created for the excitation-relaxation-emission-relaxation cycle of dye **6** (Figure 9).

The TDDFT-calculated emission at 478 nm gives rise to a Stokes shift $\Delta\nu^\sim$ of 9800 cm^{-1} . The experimentally determined Stokes shift accounts to 7700 cm^{-1} (vide supra). As expected, the experimental emission band can be assigned as fluorescence represented by the vibrationally relaxed S_1 state consisting of a HOMO→LUMO transition. Examining the coefficient density distribution of the orbitals involved in the transition from the vibrationally relaxed S_1 state to the vibrationally excited state S_0^* reveals a significant shift in coefficient density. The coefficient density distribution over the BBTT's scaffold in the LUMO (S_1) changes upon transition to HOMO (S_0^*) by concentration of the coefficient density distribution on the central 1,4-thiazine core. This agrees with a weak charge-transfer character. The significant geometric differences and the associated large energetic

differences between vibrationally excited S_1^* and vibrationally relaxed S_1 account for the experimentally determined high Stokes shift $\Delta\nu^\sim$ of 7700 cm^{-1} . On the one hand, the increase in the folding angle φ can be cited, while on the other hand, a conformational change of the sulfoxide also plays a role. In this process, the folding angle φ increases by 8°. Such an increase in the degree of planarity due to photonic excitation is also known for the parent compound **3**.^[7b] However, since in this case complete planarization occurs with a folding angle φ of $\sim 180^\circ$, the folding angle φ changes by $\sim 30^\circ$ in theory for compound **3**. Accordingly, this geometric change as the unfolding of the BBTT's scaffold is less pronounced for compound **6** than for precursor **3**. However, a similarly complete planarization was not necessarily expected for BBTT-S-oxide **6** due to the additional steric demand of the oxygen atom, restricting the system in its freedom.

If geometric differences upon photoexcitation are assumed to be the primary reason for the magnitude of the Stokes shift $\Delta\nu^\sim$, then a smaller Stokes shift $\Delta\nu^\sim$ should result for compound **6** due to the lower degree of planarization. Experimentally,

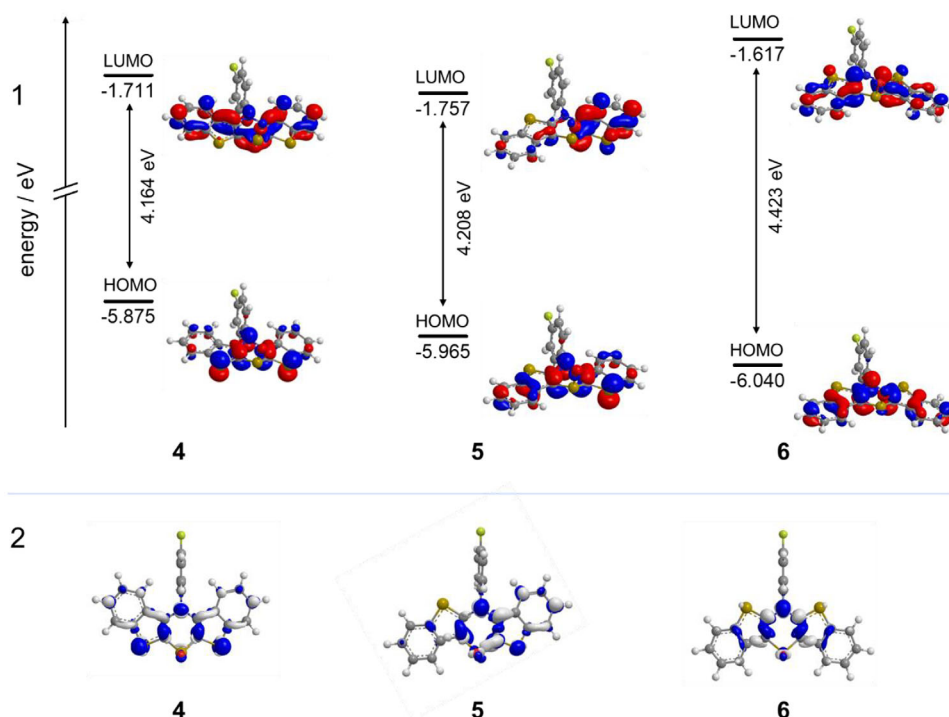


Figure 8. (1) Kohn-Sham frontier molecular orbitals (HOMO–LUMO) and their corresponding limiting orbital energies and (2) charge transfer character of $S_0 \rightarrow S_1$ transition visualized by the difference of HOMO–LUMO coefficient density (increase in white, decrease in blue) of BBTT-S-oxides 4, 5, and 6 (B3LYP/6–311++G**, IEFCPCM CH_2Cl_2 , isosurface value at 0.04 a.u. (HOMO/LUMO) and 0.002 a.u. (HOMO–LUMO overlap integral)).

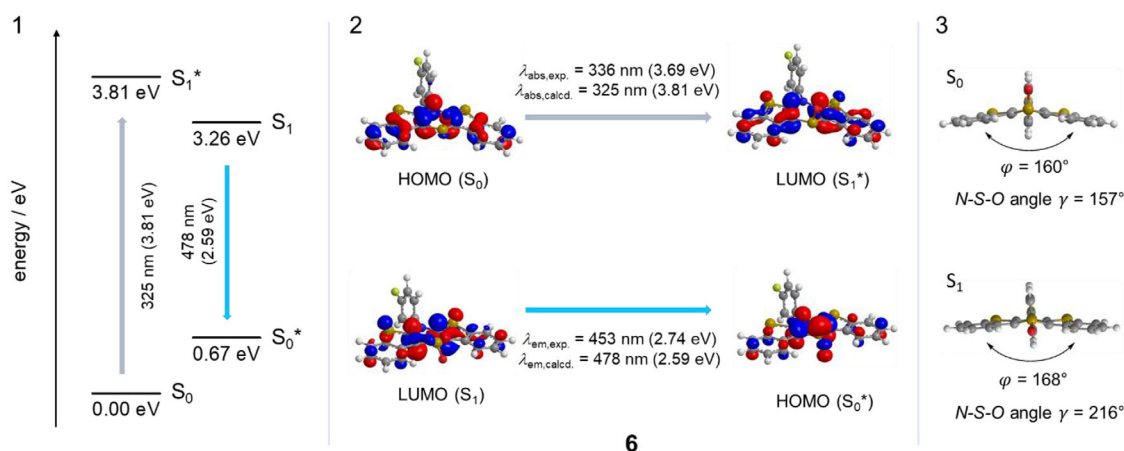


Figure 9. (1) Jablonski diagram of BBTT-S-oxide 6 based upon the TDDFT calculation (B3LYP/6–311++G**, IEFCPCM CH_2Cl_2). (2) Corresponding Kohn-Sham frontier molecular orbital geometries of the $S_0 \rightarrow S_1^*$ transition (longest wavelength absorption band) and the $S_0^* \rightarrow S_1$ transition (fluorescence band) (B3LYP/6–311++G**, IEFCPCM CH_2Cl_2) (isosurface value at 0.05 a.u.). (3) Graphical representation of the corresponding vibrationally relaxed minimum geometries of the S_0 and S_1 states in the frontal view (B3LYP/6–311++G**, IEFCPCM CH_2Cl_2).

however, the Stokes shift $\Delta\nu^-$ of 6 is actually increased by nearly 1500 cm^{-1} compared to precursor 3. This can be explained by an additional significant geometric change in compound 6 caused by the sulfoxide oxygen atom, that is, by an additional conformational change from an *S-extra* conformer of S_0/S_1^* to an *S-intra* conformer of S_1 . In this process, the N–S–O angle γ increases by 59° from 157° (S_0) to 216° (S_1). The interplay of these concomitant structural changes of the electronic structure upon relaxation jointly account for the large Stokes shift $\Delta\nu^-$.

3. Conclusion

The chemoselective oxidation of three regioisomeric *N-para*-fluorophenyl-BBTTs with copper(II) nitrate trihydrate gives rise to the formation of *syn-syn*-, *syn-anti*-, *anti-anti*-BBTT-S-oxides in moderate to good yields. Single crystal structure analyses confirm considerable planarization of the BBTTs' scaffolds with concomitant placement of the *N-para*-fluorophenyl substituent into an *N-intra* conformation, while the newly formed S-oxide

is oriented in a pseudo-axial *S*-oxide-extra position. While DFT-calculated structures indicate a diminished planarization of the BBTTs' scaffolds, a dominance of the crystal packing can be assumed for the experimentally observed widening of the folding angles. Most interestingly, the electronic properties, where the intensity of the longest wavelength absorptions is dependent on the anellation mode, that is, the most planarized *anti-anti*-BBTT-*S*-oxide displays the highest extinction coefficient $\epsilon(\lambda)$. This regioisomer also displays strong blue luminescence, both in solution and in the solid state. The absorption bands of all three regioisomers as well as the emission band of the *anti-anti*-BBTT-*S*-oxide can be nicely reproduced by TDDFT calculations, which finally allow assign their nature as HOMO–LUMO transitions. Those are minor in charge-transfer character and possess significant transition dipole moment overlap for the *anti-anti*-regioisomer. The unexpected, remarkably large Stokes shift $\Delta\nu$ of this isomer, albeit of its increased ground state planarization, can be rationalized by the considerable geometry change of the orientation of the oxide from an *S*-oxide-extra- to an *S*-oxide-intra-conformation, as seen in the calculated structure of the vibrationally relaxed S_1 state. The possibility of fine-tuning the emission characteristics of *anti-anti*-BBTT-*S*-oxide, especially by increasing extinction coefficients and fluorescence quantum yields in solution and in the solid state is highly attractive for further exploring the class of blue emitters, which is currently underway.

Supporting Information

The authors have cited additional references within the Supporting Information.^[58,59]

Acknowledgements

The authors are grateful to the Jürgen Manchot Foundation (scholarship for S. T. H.), Deutsche Forschungsgemeinschaft DFG (grant Mu 1088/9–1), and the Fonds der Chemischen Industrie for financial support.

Open access funding enabled and organized by Projekt DEAL.

Conflict of Interests

The authors declare no conflict of interest.

Data Availability Statement

The data that support the findings of this study are available in the supplementary material of this article.

Keywords: Crystal structure • Fluorescence • Oxidation • *S*-oxides • Thiazines

- [1] S. Fratini, M. Nikolka, A. Salleo, G. Schweicher, H. Sirringhaus, *Nat. Mater.* **2020**, *19*, 491–502.
- [2] C. Wang, X. Zhang, W. Hu, *Chem. Soc. Rev.* **2020**, *49*, 653–670.
- [3] H. Bronstein, C. B. Nielsen, B. C. Schroeder, I. McCulloch, *Nat. Chem. Rev.* **2020**, *4*, 66–77.
- [4] M. E. Bhosale, S. Chae, J. M. Kim, J.-Y. Choi, *J. Mater. Chem. A* **2018**, *6*, 19885–19911.
- [5] P. Bujak, I. Kulszewicz-Bajer, M. Zagorska, V. Maurel, I. Wielgusa, A. Pron, *Chem. Soc. Rev.* **2013**, *42*, 8895–8999.
- [6] H. Dong, H. Zhu, Q. Meng, X. Gong, W. Hu, *Chem. Soc. Rev.* **2012**, *41*, 1754–1808.
- [7] C.-T. Chen, *Chem. Mater.* **2004**, *16*, 4389–4400.
- [8] Y. Ahn, D. E. Jang, Y.-B. Cha, M. Kim, K.-H. Ahn, Y. C. Kim, *Bull. Korean Chem. Soc.* **2013**, *34*, 107–111.
- [9] J. K. Salunke, F. L. Wong, K. Feron, S. Manzhos, M. F. Lo, D. Shinde, A. Patil, C. S. Lee, V. A. L. Roy, P. Sonar, P. P. Wadgaonkar, *J. Mater. Chem. C* **2016**, *4*, 1009–1018.
- [10] Y. Park, B. Kim, C. Lee, A. Hyun, S. Jang, J.-H. Lee, Y.-S. Gal, T. H. Kim, K.-S. Kim, J. Park, *J. Phys. Chem. C* **2011**, *115*, 4843–4850.
- [11] C. Poriol, J. Rault-Berthelot, S. Thiery, C. Quinton, O. Jeannin, U. Biapo, D. Tondelier, B. Geffroy, *Chem. - Eur. J.* **2016**, *22*, 17930–17935.
- [12] S. Feng, Q.-S. Li, T. A. Niehaus, Z.-S. Li, *Org. Electron.* **2017**, *42*, 234–243.
- [13] T. H. Schloemer, J. A. Christians, J. M. Luther, A. Sellinger, *Chem. Sci.* **2019**, *10*, 1904–1935.
- [14] H. Bin, Y. Ji, Z. Li, N. Zhou, W. Jiang, Y. Feng, B. Lin, Y. Sun, *J. Lumin.* **2017**, *187*, 414–420.
- [15] Y. Wang, Y. Zhu, G. Xie, H. Zhan, C. Yang, Y. Cheng, *J. Mater. Chem. C* **2017**, *5*, 10715–10720.
- [16] R. Rybakiewicz, M. Zagorska, A. Pron, *Chem. Pap.* **2017**, *71*, 243–268.
- [17] K. Y. Chiu, T. T. H. Tran, C.-G. Wu, S.-H. Chang, T.-F. Yang, Y. O. Su, *J. Electroanal. Chem.* **2017**, *787*, 118–124.
- [18] J. Wang, K. Liu, L. Ma, X. Zhan, *Chem. Rev.* **2016**, *116*, 14675–14725.
- [19] E. Mondal, W.-Y. Hung, K.-T. Lin, H.-F. Chen, K.-T. Wong, *Org. Electron.* **2016**, *37*, 115–125.
- [20] L. May, T. J. J. Müller, *Chem. - Eur. J.* **2020**, *26*, 12111–12118.
- [21] L. May, T. J. J. Müller, *Chem. Eur. J.* **2020**, *26*, 12978–12986.
- [22] L. May, T. J. J. Müller, *Molecules* **2020**, *25*, 2180.
- [23] H. R. V. Berens, T. J. J. Müller, *Org. Mater.* **2021**, *3*, 155–167.
- [24] A. P. W. Schneeweis, S. T. Hauer, D. A. Lopez, B. von Dressler, G. J. Reiss, T. J. J. Müller, *J. Org. Chem.* **2019**, *84*, 5582–5595.
- [25] A. P. W. Schneeweis, S. T. Hauer, G. J. Reiss, T. J. J. Müller, *Chem. - Eur. J.* **2019**, *25*, 3582–3590.
- [26] H. R. V. Berens, K. Mohammad, G. J. Reiss, T. J. J. Müller, *J. Org. Chem.* **2021**, *86*, 8000–8014.
- [27] S. T. Hauer, P. Kuhn, J. M. Pütz, G. J. Reiss, L. P. Sorge, C. Ganter, K. Heinze, T. J. J. Müller, *Org. Chem. Front.* **2024**, *11*, 5741–5753.
- [28] S. T. Hauer, A. P. W. Schneeweis, S. D. Waniek, L. P. Sorge, K. Heinze, T. J. J. Müller, *Org. Chem. Front.* **2021**, *8*, 5744–5755.
- [29] L. Găină, A. Csámpai, G. Túrós, T. Lovász, V. Zsoldos-Mády, I. A. Silberg, P. Sohár, *Org. Biomol. Chem.* **2006**, *4*, 4375–4386.
- [30] Deposition Numbers CCDC **2345951**, **2345953**, and **2345954** contain the supplementary crystallographic data for this paper. These data are provided free of charge by the joint Cambridge Crystallographic Data Centre and Fachinformationszentrum Karlsruhe Access Structures service.
- [31] L. J. Farrugia, *J. Appl. Crystallogr.* **2012**, *45*, 849–854.
- [32] S. G. Dahl, P. A. Kollman, S. N. Rao, U. C. Singh, *J. Comput. Aided Mol. Des.* **1992**, *6*, 207–222.
- [33] X. Li, M. J. Frisch, *J. Chem. Theory Comput.* **2006**, *2*, 835–839.
- [34] P. Pulay, G. Fogarasi, F. Pang, J. E. Boggs, *J. Am. Chem. Soc.* **1979**, *101*, 2550–2560.
- [35] G. Fogarasi, X. Zhou, P. W. Taylor, P. Pulay, *J. Am. Chem. Soc.* **1992**, *114*, 8191–8201.
- [36] P. Pulay, G. Fogarasi, *J. Chem. Phys.* **1992**, *96*, 2856–2860.
- [37] J. Baker, *J. Comput. Chem.* **1993**, *14*, 1085–1100.
- [38] C. Peng, H. B. Schlegel, *Isr. J. Chem.* **1993**, *33*, 449–454.
- [39] M. J. Frisch, G. W. Trucks, H. B. Schlegel, G. E. Scuseria, M. A. Robb, J. R. Cheeseman, G. Scalmani, V. Barone, B. Mennucci, G. A. Petersson, H. Nakatsuji, M. Caricato, X. Li, H. P. Hratchian, A. F. Izmaylov, J. Bloino, G. Zheng, J. L. Sonnenberg, M. Hada, M. Ehara, K. Toyota, R. Fukuda, J. Hasegawa, M. Ishida, T. Nakajima, Y. Honda, O. Kitao, H. Nakai, T.

- Vreven, J. J. A. Montgomery, Gaussian 09, Revision A.02, Gaussian, Inc., Wallingford CT **2009**.
- [40] A. D. Becke, *J. Chem. Phys.* **1993**, *98*, 5648–5652.
- [41] C. Lee, W. Yang, R. G. Parr, *Phys. Rev. B* **1988**, *37*, 785–789.
- [42] G. A. Petersson, M. A. Al-Laham, *J. Chem. Phys.* **1991**, *94*, 6081–6090.
- [43] A. D. McLean, G. S. Chandler, *J. Chem. Phys.* **1980**, *72*, 5639–5648.
- [44] R. Krishnan, J. S. Binkley, R. Seeger, J. A. Pople, *J. Chem. Phys.* **1980**, *72*, 650–654.
- [45] T. Clark, J. Chandrasekhar, G. W. Spitznagel, P. V. R. Schleyer, *J. Comput. Chem.* **1983**, *4*, 294–301.
- [46] M. J. Frisch, J. A. Pople, J. S. Binkley, *J. Chem. Phys.* **1984**, *80*, 3265–3269.
- [47] C. F. Macrae, I. Sovago, S. J. Cottrell, P. T. A. Galek, P. McCabe, E. Pidcock, M. Platings, G. P. Shields, J. S. Stevens, M. Towler, P. A. Wood, *J. Appl. Crystallogr.* **2020**, *53*, 226–235.
- [48] P. R. Spackman, M. J. Turner, J. J. McKinnon, S. K. Wolff, D. J. Grimwood, D. Jayatilaka, M. A. Spackman, *J. Appl. Crystallogr.* **2021**, *54*, 1006–1011.
- [49] M. A. Spackman, D. Jayatilaka, *CrystEngComm* **2009**, *11*, 19–32.
- [50] C. Manual, <https://crystalexplorer.net/docs/category/isosurfaces> (accessed 17.5.2024).
- [51] G. Desiraju, T. Steiner, in *Structural Chemistry and Biology*, Oxford University Press, Oxford, **2001**.
- [52] M. Mantina, A. C. Chamberlin, R. Valero, C. J. Cramer, D. G. Truhlar, *J. Phys. Chem. A* **2009**, *113*, 5806–5812.
- [53] A. D. Laurent, C. Adamo, D. Jacquemin, *Phys. Chem. Chem. Phys.* **2014**, *16*, 14334–14356.
- [54] C. Adamo, D. Jacquemin, *Chem. Soc. Rev.* **2013**, *42*, 845–856.
- [55] G. Scalmani, M. J. Frisch, *J. Chem. Phys.* **2010**, *132*, 114110.
- [56] J. Tomasi, B. Mennucci, R. Cammi, *Chem. Rev.* **2005**, *105*, 2999–3094.
- [57] P. A. M. Dirac, *Proc. R. Soc. Lond. A* **1927**, *114*, 243–265.
- [58] M. Adam, E. Hovestreydt, M. Ruf, J. Kaercher, *Acta Crystallogr., Sect. A: Found. Adv.* **2015**, *71*, s194.
- [59] O. V. Dolomanov, L. J. Bourhis, R. J. Gildea, J. A. K. Howard, H. Puschmann, *J. Appl. Crystallogr.* **2009**, *42*, 339–341.

Manuscript received: April 23, 2025

Version of record online: June 17, 2025